

The M_w 7.1, Hector Mine, California earthquake: surface rupture, surface displacement field, and fault slip solution from ERS SAR data

Gilles Peltzer^{a,b,*}, Frédéric Crampé^{a,b}, Paul Rosen^b

^a Earth and Space Science Department, University of California, Los Angeles, CA 90095, USA

^b Jet Propulsion Laboratory, California Institute of Technology, Pasadena, CA 91109, USA

Received 21 May 2001; accepted 8 August 2001

Abstract – The M_w 7.1, Hector Mine, California earthquake of October 16, 1999 produced a 50 km-long surface rupture, ~20 km east of the surface rupture of the 1992 Landers earthquake. ERS2 radar data acquired before and after the event provide geodetic measurements of two components of the co-seismic surface displacement field. (1) Interferometric processing of the data provides the range (radar line of sight) component of the displacement field with a precision of a few millimeters. (2) The sub-pixel correlation of the before and after amplitude images provides a second component of the surface displacement field, parallel to the satellite track, with a precision of ~20 cm. The azimuth offset map reveals a ~50 km long, NNW surface rupture formed of three sections: a N40°W southern section following the Bullion fault, a N10°W central section cutting through the Bullion Mountains, and a northern N40°W section extending up to the Lavic Lake. A north-south-trending, localized gradient in the azimuth offset field suggests that the central section of the fault extends to the north at depth over a distance of ~10 km. The slip distribution curve constructed using the azimuth offsets has a bell shape, with a maximum of 6.5 m at the north end of the central fault section. The fault slip model derived from the inversion of the azimuth and range displacement data indicates that 3–5.8 m of right-lateral slip occurred between the depths of 0 and 8 km along the northern and the central sections of the fault. The solution bears a down-dip component of slip of ~2 m, west side down, along the southern part of the northern fault section. The down-dip component of slip is consistent with compression on a northeast dipping fault. © 2001 Académie des sciences / Éditions scientifiques et médicales Elsevier SAS

earthquake / Hector Mine / radar interferometry / geodesy / California

Résumé – Le tremblement de terre de Hector Mine, Californie, de magnitude 7,1 : rupture de surface, champ de déplacement et modèle de glissement sur la faille à partir de données SAR du satellite ERS. Le tremblement de terre de Hector Mine, en Californie, de magnitude 7,1, survenu le 16 octobre 1999 a produit une rupture de surface de 50 km de long, à ~20 km à l'est de la rupture du tremblement de terre de Landers de 1992. Des images radar acquises par le satellite ERS2 avant et après l'événement fournissent la mesure de deux composantes du champ de déplacement co-sismique. (1) Le traitement interférométrique des données fournit la composante le long de l'axe de visée du radar avec une précision de quelques millimètres. (2) La corrélation des images d'amplitude fournit la composante du déplacement en azimut, parallèle à la trace du satellite, avec une précision de ~20 cm. La carte des déplacements en azimut révèle une rupture de surface de ~50 km de

* Correspondence and reprints.

E-mail address: peltzer@ess.ucla.edu (G. Peltzer).

long, de direction NNW, constituée de trois sections : une section sud, de direction N40°W, une section centrale de direction N10°W, passant au travers du massif de Buillon, et une section nord, de direction N40°W, allant jusqu'au lac de Lavic. Une zone de gradient localisée de direction nord-sud suggère que la section centrale de la faille s'étende en profondeur vers le nord, sur environ 10 km. La courbe de distribution de glissement, construite à partir des données de déplacement en azimut, a une forme en cloche et atteint un maximum de 6,5 m le long de la partie nord de la section centrale de la faille. Le modèle de glissement sur la faille, calculé par inversion des deux composantes du déplacement de surface, indique qu'un glissement dextre de 3 à 5,8 m s'est produit entre 0 et 8 km de profondeur, le long des sections nord et centrale de la faille. La solution indique également une composante de glissement d'environ 2 m dans la direction du pendage de la faille, abaissant le compartiment ouest le long de la partie sud de la section nord de la faille. Une telle composante est en accord avec un régime compressif sur une faille à pendage vers le nord-est, comme le suggère la distribution en profondeur des répliques sismiques. © 2001 Académie des sciences / Éditions scientifiques et médicales Elsevier SAS

tremblement de terre / Hector Mine / interférométrie radar / géodésie / Californie

Version abrégée

1. Introduction

L'interférométrie radar est une technique d'imagerie qui permet de construire des cartes de la topographie et des déplacements de la surface de la Terre. Depuis l'avènement des systèmes radar embarqués sur satellites (principalement les satellites ERS, JERS et Radarsat, ainsi que les missions SAR de la navette spatiale), les images radar sont utilisées pour étudier de nombreux phénomènes géophysiques, comme les tremblements de terre, les volcans, les glissements de terrain et l'écoulement des glaciers. Cet article présente un exemple d'application de cette nouvelle technique à l'étude du tremblement de terre d'Hector Mine, en Californie, de magnitude 7,1, survenu le 16 octobre 1999.

2. Le tremblement de terre d'Hector Mine, Californie

Le tremblement de terre d'Hector Mine a produit une rupture de surface de 50 km de long dans la zone de cisaillement de Californie de l'Est, à environ 20 km à l'est de la rupture du séisme de Landers de juin 1992 (*figure 1*). La rupture complexe est formée de trois segments, dont certains suivent les failles quaternaires de Buillon et de Lavic. L'enregistrement sismique et les observations de terrain indiquent que la faille a produit un déplacement dextre, avec un déplacement de surface maximum de plus de 5 m.

3. Analyse des données radar

Le satellite ERS-2 de l'Agence spatiale européenne a acquis des images de la région le 15 septembre 1999, 30 jours avant l'événement, et le 20 octobre 1999, quatre jours après. Deux traitements ont été conduits : (1) un traitement interférométrique avec le logiciel ROI_PAC, développé au JPL, qui donne accès à une mesure du déplacement co-sismique dans l'axe de visée du radar,

avec une précision de quelques millimètres (*figure 2*) ; (2) la corrélation des images d'amplitude, qui fournit une estimation de la composante horizontale du déplacement de surface, parallèle à la trace du satellite au sol (*figure 3*). La précision de cette composante, dite en azimut, est d'environ 20 cm pour ce système.

4. Rupture de surface et distribution de glissement

La trace de la rupture de surface s'observe directement dans la carte des déplacements en azimut (*figure 3*). Ces données fournissent également une bonne estimation des glissements le long de la faille en surface. La distribution de glissement est bimodale, le segment principal étant situé le long de la section nord, longue de 40 km (*figure 4*). Ces observations sont en général en accord avec les observations faites sur le terrain.

5. Champ de déplacement de surface bi-dimensionnel

L'analyse des données radar par interférométrie et corrélation des images d'amplitude fournit deux composantes du champ de déplacement : l'une, précise à quelques millimètres, le long de l'axe de visée du radar, l'autre, précise à environ 20 cm, le long de l'axe de la trace au sol du satellite. La composante le long de l'axe de visée est principalement sensible aux déplacements verticaux et également à la composante horizontale, perpendiculaire à la trace du radar. L'observation de ces deux composantes montre les complexités de la rupture et des déplacements proches (*figures 2a, 3a et 5*). En accord avec la distribution des répliques sismiques, elle suggère en particulier que la rupture se divise en deux branches vers le nord, la branche est n'atteignant pas la surface.

6. Solution de glissement sur la faille en profondeur

Les deux composantes du champ de déplacement ont été inversées pour résoudre le glissement sur la faille en

profondeur. La faille est modélisée par des sections verticales planes de ~ 5 km de long et de 4 km en vertical, suivant la rupture de surface. La solution indique que le déplacement est essentiellement dextre et localisé entre les profondeurs de 0 et 8 km sur les sections centrale et nord de la faille (*figure 6*). La solution montre également une composante verticale du déplacement le long des sections au nord du point de changement abrupt de la direction de la faille (*figure 6*). Cette composante est compatible avec un mouvement chevauchant sur une faille à fort pendage vers le nord-est, comme le suggère la distribution des répliques en profondeur.

7. Conclusions

Une paire d'images radar ERS encadrant le tremblement de terre de Hector Mine a permis de cerner la rupture de surface, d'estimer la distribution de glissement en surface le long de la faille, de déterminer deux composantes du champ de déplacement sur une zone de 100 km par 200 km, et de résoudre le glissement en profondeur par inversion du champ de déplacement de surface. Ces résultats, en bon accord avec les enregistrements sismologiques et les observations de terrain, ont été obtenus dans les semaines qui ont suivi l'événement, grâce à l'acquisition et à la distribution rapide des données par l'Agence spatiale européenne.

1. Introduction

Synthetic aperture radar interferometry (InSAR) is an imaging technique providing maps of the topography and displacement of the Earth's surface. Since the advent of space borne radar instruments (essentially the European Space Agency Earth Remote Sensing Satellites (ERS), the Japanese JERS-1, the Canadian RADARSAT, and the US Shuttle radar missions), InSAR has been used to study a variety of geophysical phenomena including earthquakes, volcanic activity, ground subsidence, landslides, and glacier flow. Several reviews of the theory and applications of InSAR have been published [1, 11, 12, 18]. The principal advantage of InSAR over geodetic techniques relying on ground-based instrument arrays is to provide a spatially continuous view of the radar line-of-sight component of the surface displacement field over broad areas. This unique capability allows scientists to measure with millimeter precision surface displacement features with spatial signatures ranging from a few tens of meters to 100 km. In relatively well-instrumented regions like Southern California, InSAR is complementary to geodetic arrays using continuously operating Global Positioning System (GPS) instruments at array nodes. In addition to providing accurate line of sight change measurements, radar images also provide along-track ground displacement measurements from sub-pixel correlation of amplitude images (e.g., [2, 14]). As an example of application of the InSAR and the amplitude correlation techniques, we present here the results of the study of the $Mw7.1$ Hector Mine, California earthquake of October 16, 1999. The analysis of a single pair of ERS SAR images covering the earthquake allowed us to map the surface break produced by the earthquake and two components of the surface displacement field over an area of 120×200 km 2 , and to derive a variable slip model of the static displacement on the fault at depth.

2. The Hector Mine, California earthquake

The Hector Mine earthquake produced a N150°E, 50 km-long surface rupture within the East California Shear Zone, approximately 20 km east of the Landers earthquake surface break of June 1992 (*figure 1*). The rupture follows sections of the Lavic Lake fault in the North and of the Bullion fault in the South [6, 20]. Centroid moment tensor solution and inversion of broadband seismic data show a right-lateral sense of slip on a NNW oriented fault [3]. Field observations indicate more than 5 m of right-lateral slip along the central part of the rupture [20]. The aftershock distribution [5] follows the mapped surface break and defines a north-south alignment that lies east of the northern section of the main rupture (*figure 1*). Geodetic measurements collected at 36 stations of the Southern California Integrated GPS Network (SCIGN) were used to constrain a uniform-slip fault model with trace and dip consistent with observed ground rupture and seismic focal mechanism [7].

3. Radar data analysis

The European Space Agency ERS-2 satellite imaged the area of the earthquake on September 15, 1999, 30 days before the event, and October 20, 1999, four days after the event. The short spatial separation of ~ 25 m between the ERS orbits (interferometric baseline) and the short time interval covered by this image pair are particularly appropriate for interferometric analysis (e.g., [18]). The data were processed into an interferogram using the JPL ROI_PAC software. The topographic phase was removed using the USGS 30 m digital elevation map and the resulting surface displacement map was registered to a geographic coordinate system (*figure 2a*). The dry envi-

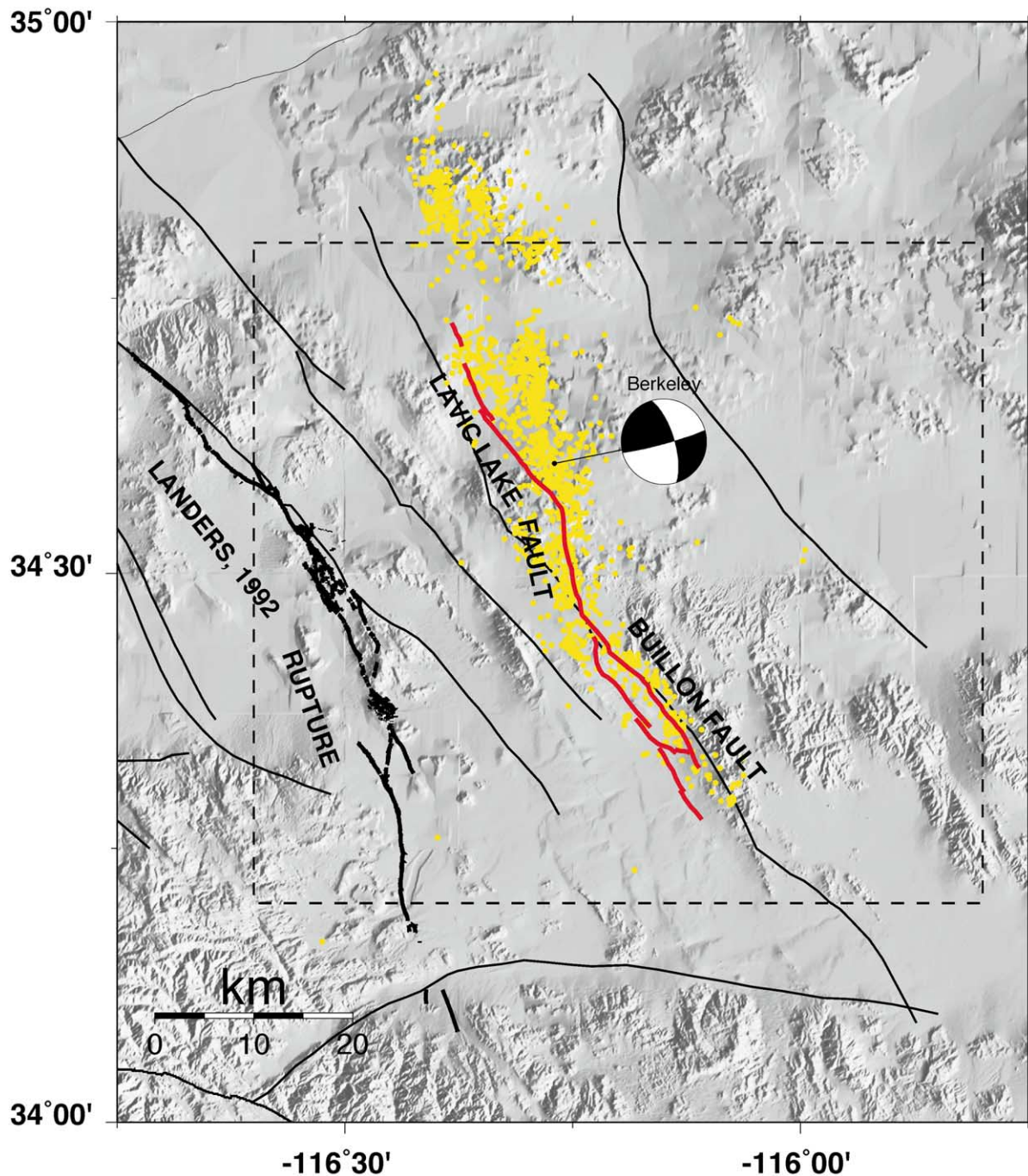


Figure 1. Fault map and seismicity associated with the Hector Mine earthquake. Yellow dots are relocated aftershocks [5]. Red, solid line is surface break produced by earthquake and mapped using azimuth offsets and phase data (see text). Black, heavy line is Landers, 1992 surface break [19]. Thin, solid lines are Quaternary faults [8]. Epicenter location and focal mechanism are shown. Dashed line box indicates area covered by figures 2a and 3a.

Figure 1. Carte de la faille et de la sismicité associées au tremblement de terre de Hector Mine. Les points jaunes sont les répliques sismiques relocalisées [5]. Les lignes rouges représentent la rupture de surface produite par le séisme et cartée à partir des données radar (voir texte). Les lignes noires et épaisses représentent la rupture du tremblement de terre de Landers de 1992 [19]. Les fines lignes noires sont les failles quaternaires [8]. L'épicentre et la solution focale sont représentés. La ligne en pointillés indique la zone couverte par les figures 2a et 3a.

ronment of the Mojave Desert, the short interferometric baseline, and the short time interval of 35 days of the image pair contributed to the high phase coher-

ence throughout the image. Except in the vicinity of the break, the interferometric phase was successfully unwrapped over the entire scene, providing an accu-

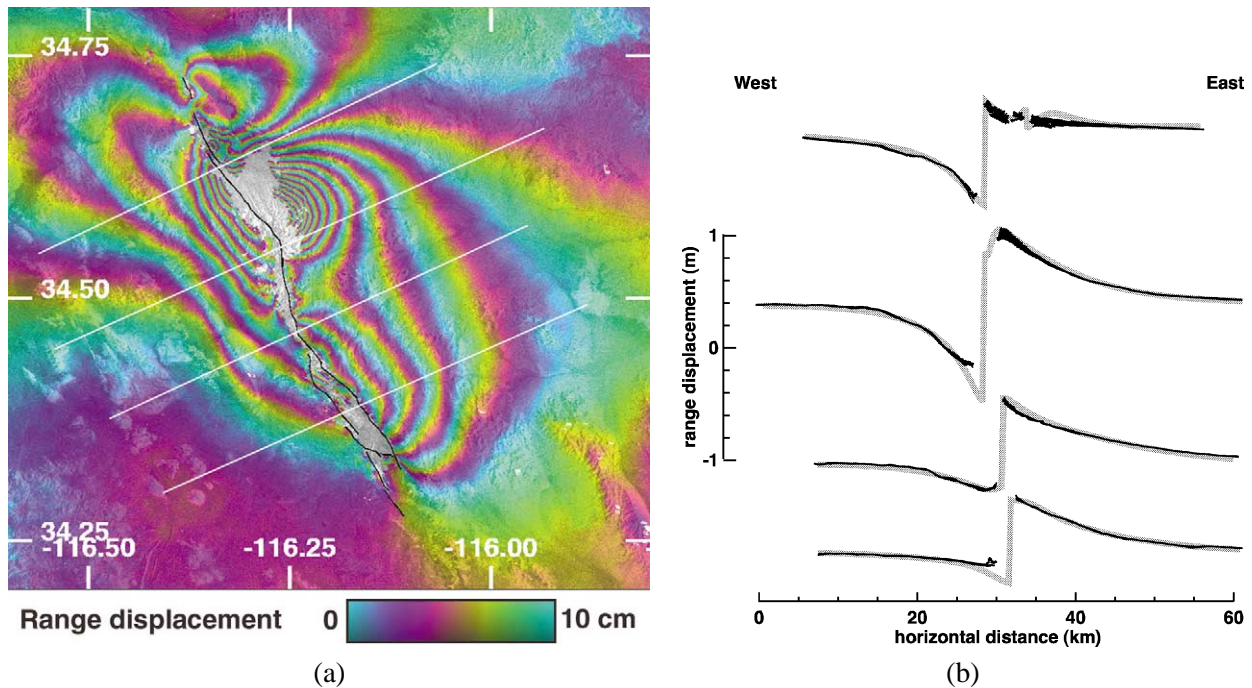


Figure 2. **a.** Interferogram formed with ERS images acquired on September 15, 1999 and October 20, 1999 showing co-seismic displacement produced by earthquake. Unwrapped interferometric phase is displayed here with one color cycle for 10 cm of ground shift parallel to radar line of sight. At latitude N34°, ERS radar is pointing at ground from an azimuth of ~N102°E and an incidence angle of 23° off nadir in center of imaged swath. Origin of displacement is arbitrary and is chosen by assuming no displacement in far field. Grey areas are zones of low phase coherence that have been masked before phase unwrapping. Solid lines represent surface breaks mapped using offset field (see text). White lines indicate location of profiles shown in *figure 2b*. **b.** Range displacement profiles perpendicular to fault (see *figure 2a* for location). Black dots are observed range displacement at image pixels within 1 km from profile axis. Gray, solid line is modeled range displacement (see text).

Figure 2. a. Interfrogramme formé à partir des images ERS acquises les 15 septembre 1999 et 20 octobre 1999, montrant le déplacement co-sismique produit par le tremblement de terre. La phase déroulée est montrée ici avec un cycle de couleur pour 10 cm de déplacement du sol dans la ligne de visée du radar. À la latitude de 34°N, le radar ERS vise le sol depuis un azimut de 102°E et un angle d'incidence de 23° par rapport au nadir au milieu de l'image. L'origine des déplacements est arbitraire et choisie en supposant un déplacement nul dans le champ lointain. Les zones en gris sont des zones de faible cohérence, qui ont été masquées avant le déroulement de la phase. La ligne noire représente la rupture de surface. Les lignes blanches indiquent la position des profils de la *figure 2b*. **b.** Profils de déplacement dans la ligne de visée du radar. Les points noirs représentent les observations aux points de l'image situés dans une bande de 1 km de large le long du profil. La ligne grise est le déplacement prédit par un modèle (voir texte).

rate measurement of the surface displacement component parallel to the radar line of sight (*figure 2*). As observed for other earthquakes associated with ground ruptures, phase coherence is low in the vicinity of the surface break. This can be attributed in part to the intense shaking of the ground disrupting surface scatterers such as small rocks and gravels, particularly in areas of steep slope (e.g., [13]), or to the high strain of the rocks adjacent to the fault reducing locally the phase coherence [14, 15]. The lowest phase coherence observed in the Hector Mine earthquake interferogram occurs in the area of steep topography of the Buillon Mountains, where the largest surface displacement is observed (*figure 2a*).

A second component of the displacement field was obtained by computing the azimuth offset field between the radar amplitude images acquired before and after the earthquake. A two dimensional offset field

is determined by sub-pixel correlation of one image to the other. It reflects the geometric shift and distortions between the two images. The azimuth component of the offset field is a measure of the surface displacement component parallel to the satellite track on the ground (*figure 3*). Typical noise in the offset fields in the present data is about 1/20th of the image pixel size, which is 4 m in the azimuth direction. The error on the azimuth offset is of the order of 20 cm. This approach is similar to the approach developed by Crippen [2] or Van Puymbroeck [21] to derive horizontal displacement fields from optical images. Except in the area of the Buillon mountains, where it appears noisy, the azimuth-offset field is coherent in the vicinity of the surface break. The combination of the interferometric phase and the azimuth offset provides us with a 2-component surface displacement field produced by the earthquake.

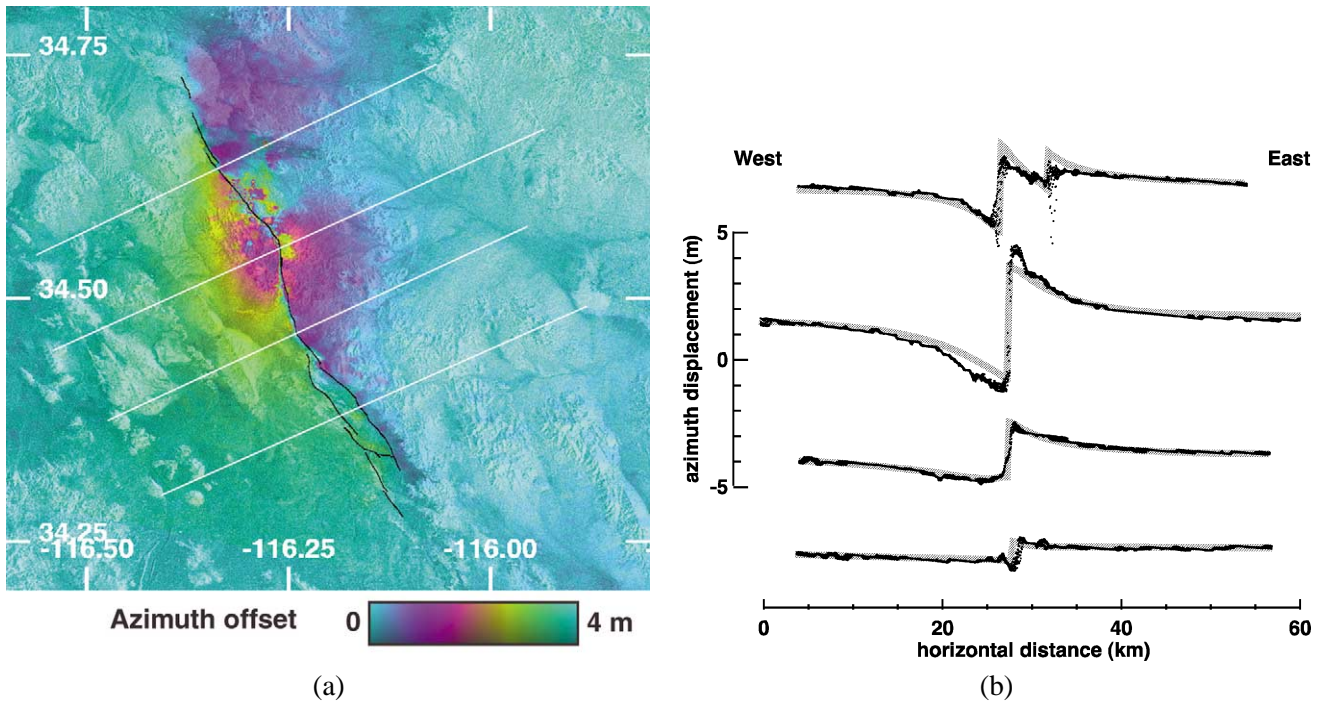


Figure 3. **a.** Azimuth component of co-seismic displacement estimated from offset field. One color cycle represents 4 m of horizontal displacement of ground parallel to satellite track direction ($N13^\circ E$). Straight lines indicate location of profiles shown in *figure 3b*. **b.** Observed (black) and modeled (gray) profiles of azimuth component of surface displacement (see *figure 3a* for location). Observed displacement at image pixels within 1 km from profile axis are represented.

Figure 3. **a.** Composante azimut du déplacement parallèle à la trace du satellite estimée à partir de la corrélation des images d'amplitude. Un cycle de couleur représente 4 m de déplacement du sol. Les lignes blanches indiquent la position des profils de la *figure 3b*. **b.** Profils de la composante en azimut du déplacement de surface observé (en noir) et modélisé (en gris).

4. Surface rupture and slip distribution

Because of its coherence in the vicinity of the fault, we used the azimuth-offset field to map the surface rupture of the earthquake (e.g., [17]). Along sections of the fault where the slip at the surface exceeds 20 cm, the fault appears as a sharp discontinuity in the offset field and can be mapped accurately (*figure 3*). Lines of phase discontinuity observed in the interferogram before phase unwrapping (not shown here) also revealed secondary fault breaks where minor slip occurred. This information was used to complement the rupture map near the northern and southern terminations of the rupture and along the western branch of the southern section of the fault. The NNW, 50 km-long surface rupture comprises three sections: a $N40^\circ W$, southern section following the Bullion fault, a $N10^\circ W$ central section cutting through the Bullion Mountains, and a northern $N40^\circ W$ section extending up to the Lavic Lake. Secondary breaks are observed in the phase data west of the southern fault section but are associated with minor displacement, barely visible in the azimuth offset (*figure 3*). The maximum right-lateral surface offset is observed at the northern end of the central section of the fault,

in the Bullion mountains and exceeds 6 m (*figure 3*). Offsets of ~ 2 m are measured along the northern section and the southern part of the central section. The main branch of the southern section shows offsets of ~ 1 m. The distribution curve of azimuth component of slip is obtained by constructing two azimuth displacement profiles on the west and east sides of the fault (*figure 4*). To avoid erroneous offset measurement near the fault where surface disruption occurred, we estimate the azimuth displacement at a distance of ~ 500 m from the fault and extrapolate the estimated value up to the fault using a linear gradient perpendicular to the fault (e.g., [17]). The displacement profiles are projected on the $N150^\circ E$ direction and the azimuth component of fault slip is the difference of the west and east profiles (*figure 4*). For a near-vertical fault the relative displacement perpendicular to the fault is negligible and the actual strike-slip component of slip is obtained by scaling the azimuth component by the inverse of the cosine of the angle between the local strike of the fault and the satellite azimuth direction (*figure 4*). The slip distribution is bimodal, with a main moment release occurring along the northern 40 km section of the fault. A second area of moment release is along the south-

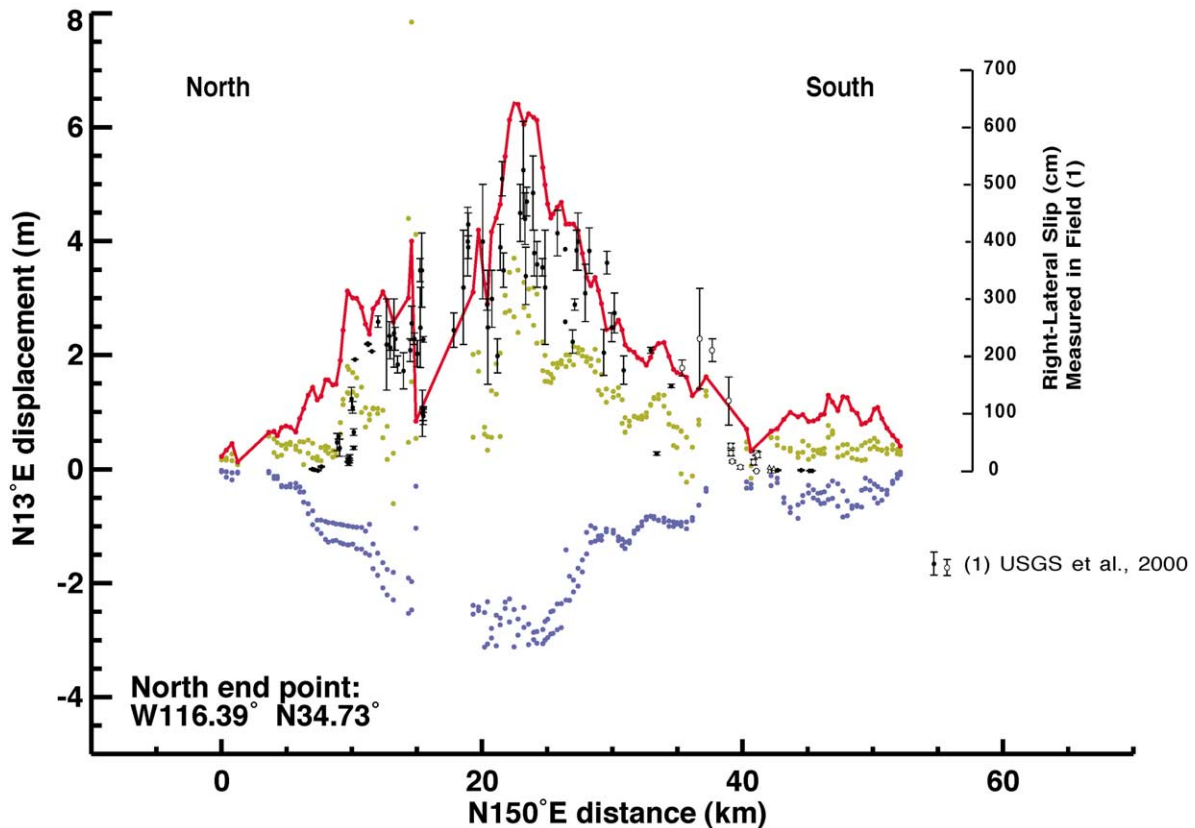


Figure 4. Azimuth displacement distribution profiles along west (blue) and east (green) sides of fault. Two dots, one for displacement value estimated ~ 500 m from fault and one for extrapolated value at fault (see text), are shown for each data point. Azimuth component of fault slip distribution (relative displacement between east and west sides) is shown in red. Assuming fault parallel displacement, fault parallel component of slip is equal to azimuth component of slip times $1/\cos\alpha$, where α is the angle between fault strike and satellite track direction ($1/\cos\alpha = 1.36$ for fault strike = N150°E). Black dots and error bars are right-lateral component of slip measured in the field [20]. Scale bar on right hand side is for field measurements.

Figure 4. Profils de la distribution de déplacement en azimut le long des côtés ouest (bleu) et est (vert) de la faille. Pour chaque point de donnée, deux points indiquent respectivement la mesure à ~ 500 m de la faille et la valeur extrapolée à la faille (voir texte). Le déplacement relatif (rouge) est obtenu par différence des courbes est et ouest. Le déplacement parallèle à la faille est égal au déplacement en azimut divisé par $\cos\alpha$, où α est l'angle entre la direction de la faille et la direction de la trace du satellite ($1/\cos\alpha = 1,36$ pour une direction de faille de N150°E). Les points noirs et le barres d'erreur sont les déplacements dextres mesurés sur le terrain [20]. L'échelle verticale à droite correspond aux mesures de terrain.

ern 17 km-long section of the fault along which the slip reached 1.1 m on the azimuth component profile (*figures 3b* and *4*). Along the northern part of the fault, the observed slip is consistent with the slip measured in the field [20], although the field observations report a maximum slip of 5.2 m, ~ 20 % less than the maximum slip observed in the radar data. Slip distributed on multiple fault branches and local wrapping near the fault may explain this discrepancy. The preliminary field studies do not report any slip along the southernmost section of the fault where the radar data indicate up to 1 m of horizontal slip [20]. It is possible that the rupture did not reach the surface along this section of the fault, producing distributed shear across a narrow zone that could not be observed in the field. However, the sharpness of the displacement feature observed in the data there indicates that the rup-

ture must be shallow along this section. Assuming a uniform slip to a depth of 8 km and a rigidity constant of $3.3 \cdot 10^{10}$ Nm for the upper crust, these observations imply a geodetic moment released by the main event of $2.6 \cdot 10^{19}$ N·m $^{-2}$, consistent with seismological observations.

We note that the displacement curves on the western and eastern sides of the fault do not depict the asymmetric pattern characteristic of non-linear elasticity that was observed in the displacement field of the Manyi, Tibet earthquake of 1997 [17]. The most likely explanation for this observation is that the subtle effect of the volume strain-dependent strength of the upper crust was identifiable in the Manyi earthquake surface displacement data because of the simple linear geometry of the fault, compared to the geometry of the Hector Mine fault. The Hector Mine

fault is a complicated rupture with abrupt changes in strike and dip between the three sections, a geometry that has a strong influence on the near-field surface displacement [4], preventing the observation of more subtle strain patterns such as those produced by nonlinear elasticity.

5. Two-component surface displacement field

The interferometric phase and the azimuth displacement provide two components of the surface displacement field produced by the earthquake (*figure 5*). The range component of the field is sensitive to vertical displacement due to the incidence angle of 23° in the center of the radar swath, and to horizontal displacement perpendicular to the satellite track. The azimuth component of the field is the horizontal displacement parallel to the satellite track ($N13^\circ E$). The overall displacement field is consistent with a right-lateral strike-slip dislocation and bears complicated patterns near the fault due to its particular geometry. A striking feature of this displacement field is the asymmetry between the two sides of the northern section of the fault (Lavic Lake fault). As the western block adjacent to the fault appears to have moved to the north with relatively small internal de-

formation near the area where the fault changes direction (at $N34.6^\circ$, *figure 1*), internal deformation seems to have occurred in the eastern block along the Lavic Lake fault (*figure 5*). The absence of phase coherence (*figure 2*) and the concentration of aftershocks [5] east of the fault also attest to distributed deformation in this compartment, which was recognized as a zone of complicated rupture by field observers [20]. The azimuth displacement field shows a sharp gradient consistent with right-lateral shear along a north–south trend extending the central section of the main rupture to the north beyond the kink point on the fault at latitude $N34.6^\circ$. This observation suggests that the central section of the surface break extends at depth toward the north over a distance of ~ 10 km. The profile in the azimuth displacement field across this zone indicates that the fault almost reached the surface along this trend with a slip of about 80 cm (*figure 3b*). Large range decrease observed on the east side of the fault at this latitude attests to vertical uplift (*figure 2*). Surface uplift there may result from the abrupt change of the main fault direction at latitude 34.6° , implying a compressive regime along the section of the main fault just north of the kink. Surface uplift east of the fault in a compressive regime would imply a northeast dip of the fault and a down-dip, west side down, component of slip.

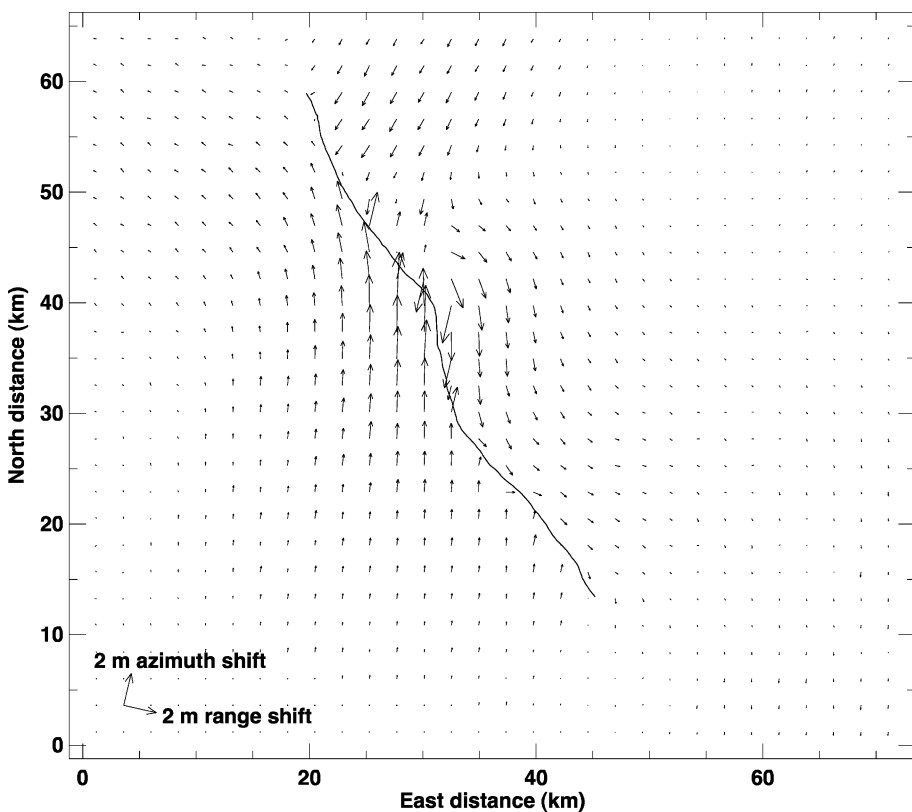


Figure 5. Field of range-azimuth displacement vectors shown on a geographic projection. Solid line indicates simplified surface rupture reference.

Figure 5. Champ des vecteurs déplacement à deux composantes (ligne de visée et azimut), représentés dans une projection géographique. La ligne noire représente la rupture de surface.

6. Sub-surface fault slip solution

We resolve the slip distribution at depth associated with the earthquake by inversion of both the azimuth and range displacement data using a singular value decomposition approach (e.g., [10]). The fault is modeled as a vertical dislocation buried in an elastic half-space [16]. We adopted a simplified fault geometry based on the fault map derived from the radar data (figure 2) and divided the fault into eleven, ~5 km-long patches over its entire length and five, 4 km-wide patches in the vertical dimension. An additional fault section was added along the shear trend extending to the north the central section of the fault. To save computer time, the data were disseminated to a total of 1 252 points by adjusting the local density of sampling to the local displacement gradient throughout the scene. The inversion minimizes the weighted quadratic difference between the observed and modeled displacement in both the range and azimuth directions.

imath directions and solves for the strike-slip and down-dip components of the slip vector on individual fault patches. The range and azimuth components of the displacement were weighted by the standard deviation values of 3 and 20 cm, respectively. The solution shown in figure 6 was obtained by retaining 48 singular values and no additional smoothing constraint was applied to the solution. Comparison between predicted and observed displacement along profiles perpendicular to the fault shows the overall good performance of the inversion (figures 2b and 3b). The largest misfits are observed near the rupture and reflect the simplified fault geometry and patch size. For example, excessive range displacement modeled west of the fault along the second profile from north may be due to the fact that the fault section just north of the fault kink is modeled as a vertical fault and not a steeply northeast-dipping fault. Misfits observed along the azimuth profiles in the north are probably due to the crude description of the fault with a patch

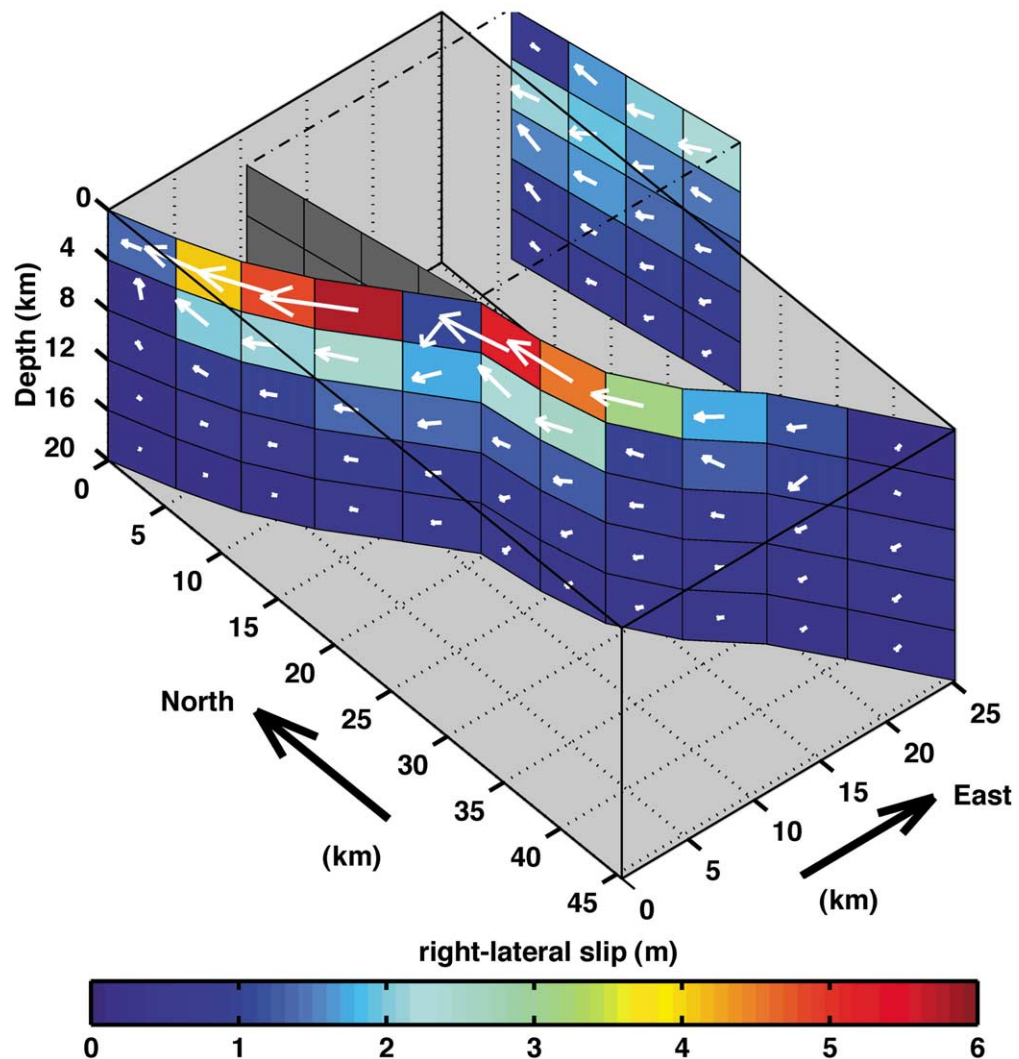


Figure 6. Fault slip solution obtained by inversion of range and azimuth displacement data. Color bar indicates magnitude of right-lateral component of slip. Arrows are slip vectors resolved on each fault patch and depict both horizontal and down-dip components of slip of western compartment with respect to eastern compartment.

Figure 6. Modèle de glissement sur la faille, obtenu par inversion des données des deux composantes de déplacement. La barre de couleur indique l'amplitude de la composante de glissement dextre. Les flèches sont les vecteurs glissement résolus sur les éléments de faille et indiquent les composantes horizontale et verticale du glissement du compartiment ouest par rapport au compartiment est.

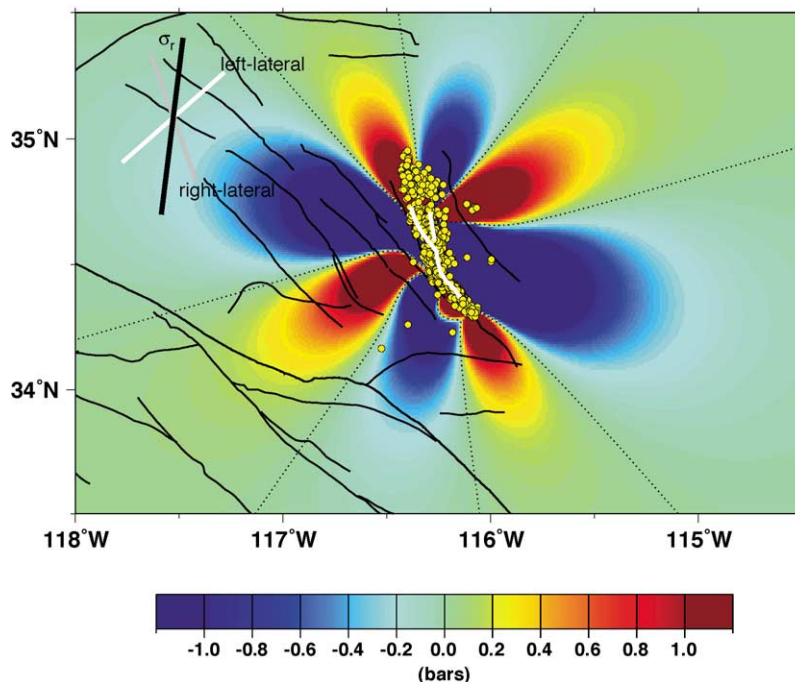


Figure 7. Coulomb stress changes caused by the Hector Mine earthquake on optimally oriented slip planes. Regional stress is chosen as a N7°E compression of 100 bar and effective friction coefficient is 0.4 [9]. Fault break is shown in white. Aftershocks [5] are shown in yellow.

Figure 7. Changements de la contrainte de Coulomb produits par le séisme de Hector Mine sur des plans verticaux orientés de manière optimale. La contrainte régionale est choisie à 100 bar et de direction N7°E, la friction effective à 0,4 [9]. La rupture est représentée en blanc, les répliques sismiques [5] en jaune.

size of 5 km, too coarse to account for high frequency variations of the displacement field along the northern sections of the fault. The solution indicates that most of the displacement occurred between depths of 0 and 8 km on the central and northern sections of the fault, where large slip is observed at the surface. Up to 2.2 m of slip is resolved on the additional north-south fault branch, east of the Lavic Lake fault. The patches of the main fault where the right-lateral slip exceeds 5 m correspond to the two maxima observed in the fault slip distribution, 13 and 23 km south of the northern end point, respectively (*figure 4*). The solution is essentially strike-slip on most of the patches, except north of the kink where the down-dip (west side down) component of slip reaches 2 m. The down-dip component of slip on this part of the fault is consistent with horizontal compression on a northeast-dipping fault plane. These findings are in agreement with the distribution of aftershocks at depth, which defines a steeply northeast-dipping fault plane along the compressive section of the Lavic Lake fault [5].

The fault solution has been used to compute the Coulomb stress change in the area around the fault [9]. Most of the aftershocks fall in areas of Coulomb stress increase (*figure 7*) with a notable exception. The swarm of aftershocks extends north of the rupture, over a distance of ~20 km. A number of them occurred on and north of the blind segment of the fault, east of the main surface break (*figures 1* and *7*). However, the magnitude of the dextral slip that is resolved on this segment does not exceed 2.5 m and

does not compensate for the stress change produced by the slip on the main rupture to the west. Many of the aftershocks associated with the blind fault segment fall in the region of stress shadow of the main rupture, following a pattern not predicted by the Coulomb criteria [9]. It is possible that our fault model is not well constrained in the north. A trade off between the two northern branches of the fault or the imposed condition of verticality of the fault plane may explain the poor prediction of the model there.

7. Conclusion

A single pair of ERS radar images covering the Hector Mine earthquake epicentral area provided us with a continuous view of two components of the surface displacement field associated with the event. The range component of the field is slanted at an angle of 23° off the vertical in a direction N103°E, and is estimated with a precision of a few millimeters from the interferometric phase. The azimuth component of the displacement field is horizontal, parallel to the N13°E direction, and estimated with a precision of ~20 cm from the azimuth offsets between the two images. The coherence of the azimuth offset field in the vicinity of the fault allowed us to map the surface rupture over its length of ~50 km and to determine the distribution of slip along the fault at the surface. The fault map and the slip distribution derived from the radar data are in overall agreement with observations gathered in the field. However, the radar data imply

a surface slip along the fault that is in general 10–20 % larger than the slip measured in the field [20]. This difference may be due to the fact that estimates from the radar data integrate possible distributed displacement and ground wrapping in the vicinity of the main rupture that are difficult to quantify in the field.

The sub-surface fault slip solution determined by inversion of the two components of the displacement field shows that slip essentially occurred between the surface and the depth of 8 km along the northern and central branches of the fault. Up to 2 m of down-dip slip (west side down) is resolved along the northern branch of the fault, north of the point where the fault strike changes by $\sim 30^\circ$. Such a down-dip component

of slip is consistent with a compressive regime on a northeast dipping fault, a geometry that is suggested by the aftershock distribution at depth [5].

The rupture and surface displacement maps of the Hector Mine earthquake were derived from a single pair of ERS images in the weeks following the event thanks to the rapid data acquisition and distribution by the European Space Agency. The analysis presented here as well as the recent examples of application of InSAR to the study of earthquakes show the level of precision achievable in mapping ground ruptures and measuring surface displacement from radar images. The rapidity of data acquisition and analysis after a major event are essential to support field deployments and monitor short-term post-seismic processes.

Acknowledgements. The ERS data were provided by the European Space Agency. We thank J.-P. Avouac and R. Michel for insightful reviews of the manuscript. The work described in this paper was performed in part at the Jet Propulsion Laboratory, California Institute of Technology, under contract with NASA.

References

- [1] Burgmann R., Rosen P.A., Fielding E., Synthetic aperture radar interferometry to measure Earth's surface topography and its deformation, *Annu. Rev. Planet. Sci.* 28 (2000) 169–209.
- [2] Crippen R., Measuring of subresolution terrain displacements using SPOT panchromatic imagery, *Episodes* 15 (1992) 56–61.
- [3] Dreger D., Kaverina A., Seismic remote sensing for the earthquake source process and near-source strong shaking: a case study of the October 16, 1999 Hector Mine earthquake, *Geophys. Res. Lett.* 27 (13) (2000) 1941–1944.
- [4] Fialko Y., Simons M., The complete (3-D) surface displacement field in the epicentral area of the 1999, Mw 7.1, Hector Mine earthquake from space geodetic observations, *Geophys. Res. Lett.* 28 (16) (2001) 3063–3066.
- [5] Hauksson E. et al., Overview of the 10/16/1999 Mw 7.1 Hector Mine, California earthquake sequence, in: *Hector Mine Earthquake Spec. Sess.*, AGU Fall Meeting, Dec. 1999.
- [6] Hector Mine Earthquake Geologic Working Group, Ponti D.J., Bryant W.A., Rockwell T.K., Kendrick K.J., Surface rupture, slip distribution and other geological features associated with the Hector Mine earthquake of 16 October, 1999, in: AGU Fall Meeting, Dec. 1999.
- [7] Hurst K.J., Argus D.F., Donnellan A. et al., The coseismic geodetic signature of the 1999 Hector Mine Earthquake, *Geophys. Res. Lett.* 27 (17) (2000) 2733–2736.
- [8] Jennings X., Fault map of California, California Division of Mines and Geology, 1974.
- [9] King G.C.P., Stein R.S., Lin J., Static stress changes and the triggering of earthquakes, *Bull. Seismol. Soc. Amer.* 84 (1994) 935–953.
- [10] Larsen S.C., Geodetic measurement of deformation in southern California, PhD thesis, California Institute of Technology, Pasadena, 1991, 351 p.
- [11] Madsen S.N., Zebker H.A., Imaging radar interferometry, in: *Principles and applications of imaging radar, Manual of remote sensing*, 2nd ed., Wiley, New York, 1999, pp. 2:359–2:380.
- [12] Massonnet D., Feigl K.L., Radar interferometry and its application to changes in the Earth's surface, *Rev. Geophys.* 36 (4) (1998) 441–500.
- [13] Massonnet D., Rossi M., Carmona C. et al., The displacement field of the Landers earthquake mapped by radar interferometry, *Nature* 364 (6433) (1993) 138–142.
- [14] Michel R., Avouac J.-P., Taboury J., Measuring ground displacements from SAR amplitude images, application to the Landers earthquake, *Geophys. Res. Lett.* 26 (1999) 875–878.
- [15] Michel R., Avouac J.-P., Taboury J., Measuring near field coseismic displacements from SAR images: application to the Landers earthquake, *Geophys. Res. Lett.* 26 (1999) 3017–3020.
- [16] Okada Y., Surface deformation due to shear and tensile faults in a half-space, *Bull. Seismol. Soc. Am.* 75 (4) (1985) 1135–1154.
- [17] Peltzer G., Crampé F., King G., Evidence of nonlinear elasticity of the crust from the Mw 7.6 Mani (Tibet) earthquake, *Science* 286 (5438) (1999) 272–276.
- [18] Rosen P.A., Hensley S., Joughin I.R. et al., Synthetic aperture radar interferometry, *Proc. IEEE* 88 (3) (2000) 333–382.
- [19] Sieh K., Jones L., Hauksson E. et al., Near-field investigation of the Landers earthquake sequence, April to July 1992, *Science* 260 (5105) (1993) 171–176.
- [20] US Geological Survey, the Southern California Earthquake Center, and the California Division of Mines and Geology, Preliminary Report on the 16 October 1999 Mw 7.1 Hector Mine, California Earthquake, *Seismol. Res. Lett.* 71 (2000) 11–23.
- [21] Van Puymbroeck N., Michel R., Binet R., Avouac J.-P., Taboury J., Measuring earthquakes from optical satellite images, *Appl. Opt.* 39 (2000) 3486–3494.